Applied Surface Science 689 (2025) 162455

Contents lists available at ScienceDirect

Applied Surface Science

journal homepage: www.elsevier.com/locate/apsusc

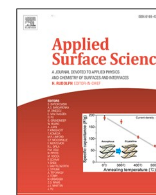

Full Length Article

Schottky contact modulation at a-GeSe/TiN interface for ovonic switching selectors

Amine Slassi [a,b], Francesco Tavanti [a,c,*], Sergiu Clima [d], Daniele Garbin [d], Arrigo Calzolari [a]

[a] CNR-NANO Research Center S3, Via Campi 213/a, Modena 41125, Italy
[b] LIRBEM, Cadi Ayyad University, ENS, Marrakech, 40000, Morocco
[c] COMT – Centre for Molecular and Translational Oncology & Department of Chemical and Life Sciences and Environmental Sustainability, University of Parma, Parco Area delle Scienze 11/A, Parma 41123, Italy
[d] IMEC, Kapeldreef 75, B-3001 Leuven, Belgium

ARTICLE INFO

Keywords:
Ohmic contact
Schottky Contact
DFT
Heterostructure
Amorphous chalcogenides

ABSTRACT

The use of amorphous GeSe-based chalcogenides in ovonic threshold switching selectors for highly efficient phase-change memory devices involves the formation of contacts with metal electrodes, where the nature of interfacial contact plays a crucial role in controlling the power efficiency. Here, by using a joint experimental-theoretical approach we study the key contact properties between TiN-electrode and amorphous GeSe (a-GeSe) semiconductor. Two types of stackable devices with and without amorphous carbon (a-C) interlayer film were investigated; namely, TiN/a-GeSe and TiN/a-C/a-GeSe stacks. The interfacial contact between TiN electrode and a-GeSe is characterized by a high Schottky barrier height (SBH) type contact. The insertion of the Carbon buffer layer develops a lower SBH with a-GeSe, leading to a higher leakage current and a lower V_{TH}, in line with the experimental observation.

1. Introduction

Chalcogenide alloys have been attracting interest as optimal materials for the realization of three-dimensional (3D) stackable memories with crossbar array architecture [1–6]. While the family of Germanium-Antimony-Tellurium (GST) compounds has been identified as testbed materials for reversible non-volatile phase-change memories (PCMs) [7–10], Germanium-Selenide (GeSe) alloys have been considered for selector elements [11], which control the accessibility and quality of data transmission inwards and outwards the 3D memory cell. The importance of GeSe stems from its high amorphous stability with a high crystallization temperature up to ~350 °C [12–14], as well as from its Ovonic Threshold Switching (OTS) behavior [15]. The latter is the capability of switching from a high-resistance (OFF) state to a low-resistance (ON) state, when a *threshold voltage* (V_{TH}) is exceeded and to recover a high-resistance (OFF) state as the applied voltage falls below the so-called *holding voltage* (V_H).

Integration of amorphous GeSe in a stackable OTS-based memory architecture inevitably involves a direct contact with metallic electrodes, which may cause unusual interface phenomena driving the device efficiency. In particular, OTS-based selectors are typically constituted of metal/insulator/metal (M/I/M) stacks, where chalcogenides are vertically connected to metallic electrodes, such as TiN [16], Pt [13], Ag [17], Ti [16]. Here, we focus on TiN/a-GeSe/TiN heterostructures [18], as prototypes of OTS selectors. Despite the simple structure, their implementation is still suffering from unstable interfacial chemical compositions and uncontrollable SBH at the interface. One prominent flaw reported in TiN/OTS/TiN devices is the titanium diffusion from TiN-electrode into chalcogenide layer, which increases the SBH and deteriorates the performance of device [16,19]. Experimental trial/error attempts indicate that Ti diffusion can be suppressed by inserting a thin carbon layer between the GeSe channel and the TiN leads in a vertical TiN/a-C/a-GeSe configuration [19]. The resulting structure exhibits a remarkable suppression of the leakage current to 10 pA and an endurance of 10^9 cycles [19]. Another approach to prevent Ti-diffusion at the interface, is to create a Se-deficient $Ge_xSe_{(1-x)}$ active layer [16]. For instance, Kim et al. fabricated a TiN/GeSe interface and demonstrated that the formation of a Ti—Se layer at the interface affects the electroforming-free bipolar resistive switching behavior, improving retention and cycling endurance. This effect is mainly associated with

* Corresponding author.
E-mail address: francesco.tavanti@unipr.it (F. Tavanti).

https://doi.org/10.1016/j.apsusc.2025.162455
Received 25 November 2024; Received in revised form 9 January 2025; Accepted 17 January 2025
Available online 29 January 2025
0169-4332/© 2025 The Author(s). Published by Elsevier B.V. This is an open access article under the CC BY-NC-ND license (http://creativecommons.org/licenses/by-nc-nd/4.0/).

the stabilization in the composition of GeSe during the electrical switching cycles, by hampering a large Se migration into the TiN electrode [16]. On the other hand, Ahn et al. demonstrated that the scaling down the thickness of amorphous a-GeSe below 40 nm, in Pt/GeSe/Pt device configuration, results in the reduction of the threshold voltage [13], which is mainly associated with the value of the SBH formed at the interface.

Although many efforts have been devoted to investigate OTS materials there is no systematic characterization of the interface between a-GeSe active channels and TiN-electrodes. While it is evident that the interfaces play a crucial role on the electrical performances of the selector, its microscopic interpretation is far from being understood. Previous works on ultra-thin films (< 10 nm) and emerging 2D materials for low-power nano-electronic devices and for catalysis showed that computer simulations are able to describe in detail the mechanisms at the interfaces complementing the experimental description [20–25].

Here, we provide a joint theoretical/ experimental investigation of these interfaces, providing a microscopic description of the SBH and its modulation upon the inclusion of a-Carbon interlayers. First, by using simulations from first principles, we characterize the three interfaces (namely TiN/a-GeSe, TiN/a-C and a-GeSe/a-C) that occur in the experimental TiN/OTS/TiN samples. We considered a-GeSe with the $Ge_{50}Se_{50}$ composition, which has been demonstrated to exhibit a very high stability over several cycles of switching [26]. The well-defined mobility gap with few trap states of stoichiometric $Ge_{50}Se_{50}$ compound [26–28] allows us for a fundamental understanding of the microscopic origin of the SHB at the interface and a direct comparison with previous experimental results [26,28].

Then, we fabricate and characterize two sets of two-terminal devices, namely TiN/GeSe(20 nm)/TiN (M/I/M) and TiN/a-GeSe(20 nm)/a-C(6 nm)/TiN (M/I/M/M). Electrical measurements are carried out to extract the key device parameters including I-V characteristics. Our results demonstrate that the TiN substrate forms a Schottky-like barrier with a-GeSe. The interface at a-C/a-GeSe heterostructure is characterized by a low Schottky barrier, which is suitable for interfacial transport of carriers. This confirms that the inclusion of carbon interlayer stabilizes the stack, blocking the Ti-diffusion without degrading the electrical performances of the selector.

2. Methods

2.1. Computational details

The calculations were performed by using the QuantumEspresso suite of codes, based on the density function theory (DFT) [29]. The electron–ion core interactions were treated by employing ultrasoft pseudopotentials [30]. Single Kohn-Sham particle wavefunctions were expanded in a planewave basis set within a kinetic energy cutoff of 30 Ry (the kinetic energy cutoff for charge density was set to 300 Ry. Since the van der Waals (vdW) interactions have been demonstrated to have a significant impact on the atomic structure of chalcogenide amorphous materials [31], we described the exchange–correlation functional interactions by using the vdW-DF-optB86b functional [32,33]. A Broyden–Fletcher–Goldfarb–Shanno (BFGS) quasi-newton algorithm was employed to relax the ions to the ground states with a total energy convergence of 10^{-4} eV, while the convergence threshold for self-consistency was set to 10^{-8} eV; the residual forces acting on each ion are less than 0.03 eV/Å, respectively. Integrations over the Brillouin zone were sampled at the Γ-point only. The degree of localization of the electronic orbitals states was evaluated by using the Inverse Participation Ratio (IPR) of the Kohn-Sham eigenstates [34].

2.2. Model system preparation

The simulated heterostructures are simulated by using periodically repeated supercells. Interface structures are constructed by combining an amorphous layer of a-GeSe with stoichiometric composition, i.e. $Ge_{50}Se_{50}$, (two considered thicknesses: 1 nm and 3 nm), one a-Carbon layer (3 nm) and a metallic TiN surface slab, with lateral dimensions (16.98×16.98) nm^2 for TiN(100) and (15.59×15.09) nm^2 for TiN (111), see Fig. 1. Slab replicas are separated by a 20 Å-thick layer of vacuum along the z-direction, perpendicular to the interface, while a dipolar correction is included to avoid the effect of the vacuum electric field, due to inequivalent surface terminations.

The initial atomic structures of amorphous a-GeSe and a-C were built by using classical MD simulations as implemented in the LAMMPS package [35] and following the same procedure reported by Tavanti et al. [14,36]. The Vashishta potential [36] and Tersoff potential [37] were used to describe the Force Field for a-GeSe and a-C amorphous structures, respectively. A simulation box including 4480 atoms was first melted for 10 ns at 1500 K and then slowly cooled down to 300 K with a cooling rate of 5 K/ps. This ensures a balance between affordable computational costs and a proper description of the amorphous structures. Then, a production run of 50 ns at 300 K was carried out in a NVT ensemble level where the temperature is controlled by the Nosé-Hoover thermostat with a coupling time of 1 fs and the timestep of 1 fs.

In order to obtain the small slab sizes to match the dimension of the crystalline TiN substrate for DFT calculations, we applied a “cutting” procedure on the MD box of amorphous systems resulting from classical MD simulations. Then, each slab was equilibrated running a second classical MD simulation at 300 K for 10 ns so as to rearrange the frustrated bonds caused by the new periodic boundary conditions. Lastly, the atomic structure of both a-GeSe and a-C were relaxed at the DFT level. The combination of the resulting structures was used to generate the initial interface geometries that were further optimized at the DFT level. The multistep cutting-procedure is described in detail in [27,38]. For convergence tests, structural and electronic properties of clean TiN surfaces we refer the reader to previous Refs [39,40].

2.3. Device fabrication and electrical characterization

Two sets of OTS devices were fabricated on 300 mm wafers using a CMOS-compatible process. The device structure consists of a bottom electrode (BE), an OTS layer, and a top electrode (TE), deposited *in-situ* via Physical Vapor Deposition (PVD) without vacuum break. The active stack was patterned into 65 nm diameter confined pillars using Reactive Ion Etching (RIE) and integrated between two metallization layers, enabling electrical access to both BE and TE. The experimental film compositions with TiN and a-C electrode materials turned-out slightly Ge-rich ($Ge_{60}Se_{40}$). However, considering that Ge-rich GeSe films increase leakage currents while they decrease the mobility gap and threshold voltage [26,41], the experimental measurements represent the worst-case scenario, with a lower mobility gap/ Schottky barrier and therefore a higher leakage, generally following predictable trends in electrical properties. The material and thickness details of the device stacks are summarized in Table 1 and a graphical sketch of the device is reported in Fig. 1. Further electrical results relative to quasi stoichiometric GeSe compounds are available for comparison in Ref [26].

Devices underwent an electrical initialization using two consecutive triangular pulses, (5 V peak, 100 ns rise/fall time), generated by an Agilent 81110A pulse generator. Subsequent I-V characteristics were measured using a K2602A Keithley Source Measure Unit (SMU). A minimum of 7 devices per wafer ID were tested, and the median characteristics are reported.

3. Results and Discussion

3.1. First principles simulations

We divided the full heterostructure in its constituent bilayer interfaces: TiN/a-GeSe, a-GeSe/a-C, and TiN/a-C. We generated interfaces composed of 3 nm-thick-slabs of amorphous a-GeSe and/or a-C

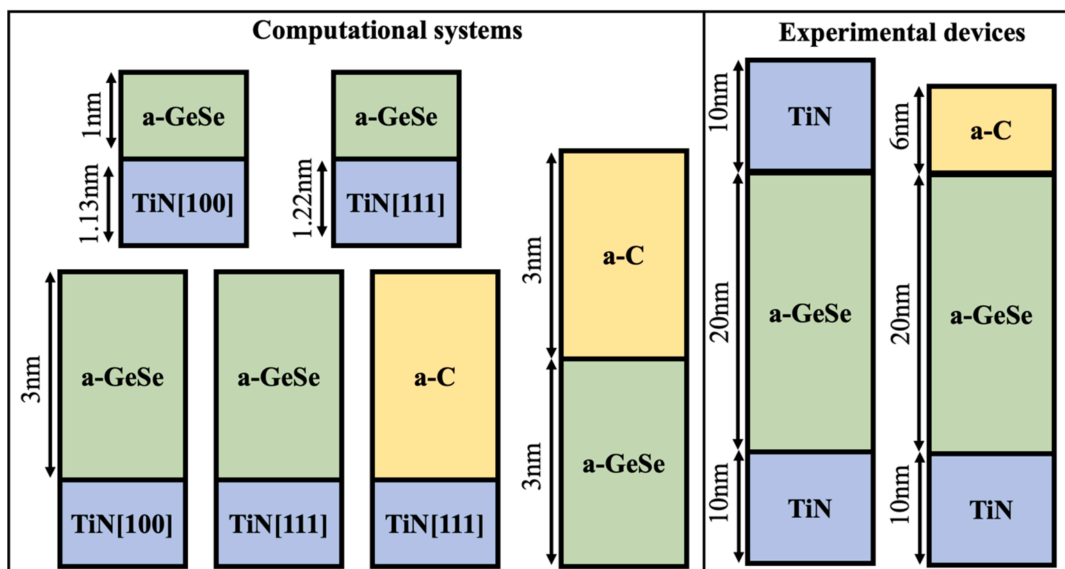

Fig. 1. Sketch of the computational systems and experimental devices employed in this work with their relative size.

Table 1
Composition and thickness of the active device stacks.

Wafer ID	BE	OTS	TE
1	10 nm TiN	20 nm $Ge_{60}Se_{40}$	10 nm TiN
2	10 nm TiN	20 nm $Ge_{60}Se_{40}$	6 nm C

materials. For the sake of completeness, we also considered an amorphous a-GeSe layer with a thickness of 1 nm, in order to study the effect of thickness on the overall interface properties.

The crystalline TiN substrates were modeled by simulating the two most favored cleavage surfaces, namely, Ti-terminated TiN(111) and TiN(100) facets [42], with rectangular areas of (16.98x16.98) nm^2 and (15.05 × 15.60) nm^2, respectively. We used 6-layer Ti/N atoms with a thickness of 11.3–12.2 Å, which are found to be sufficient to converge the work function of TiN slabs to bulk value [40]. The relaxed isolated layers used in the DFT calculations are depicted in Fig. 2**a-b** (see also **Fig. S1** of Supporting Information).

The amorphous layers were stacked on the TiN(111) and TiN(100) surfaces forming the a-GeSe/TiN, and a-C/TiN heterostructures, while the a-GeSe/aC interface resulted in combining the two amorphous

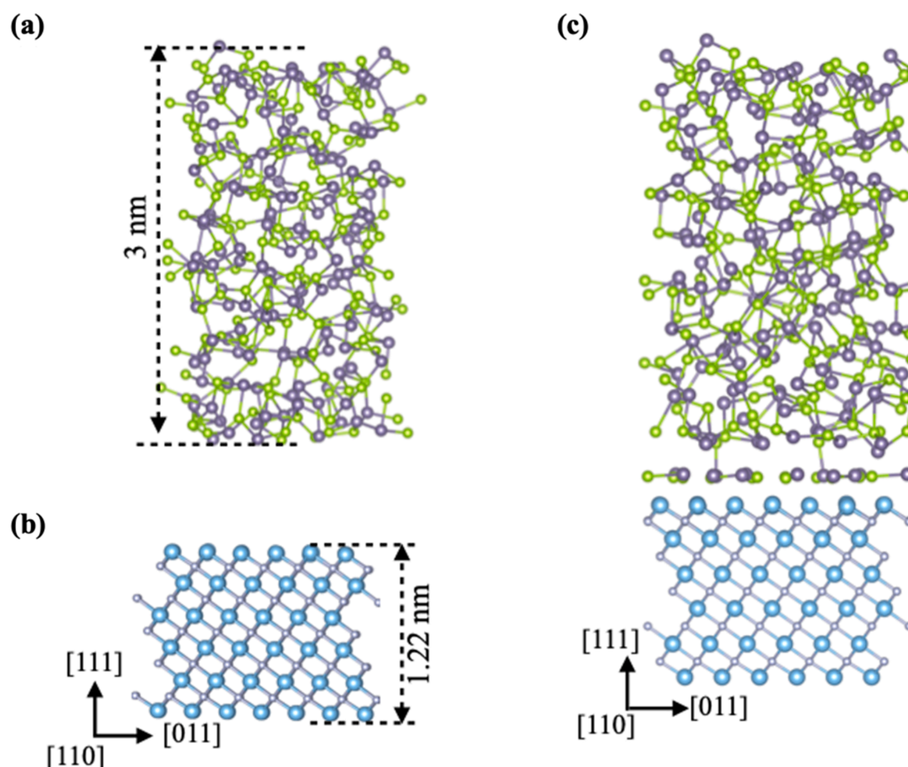

Fig. 2. Side views of representative equilibrium geometries: (a) isolated a-GeSe slab with a thickness of 3 nm, (b) isolated TiN(111) substrate with a thickness of 1.22 nm, (c) TiN(111)/a-GeSe heterostructures after DFT relaxation. Ge atoms are represented in violet, Se in green, Ti in blue and N in gray.

layers. Fig. 2**c and Fig. S2** show the side views of the equilibrium configurations of interfaces after structural optimizations.

The coupling between amorphous materials and TiN substrate causes a significant geometrical rearrangement of the atomic-layers close to the interface. For TiN(111)/a-GeSe stack, the Ge and Se atoms close to the interface region form a planar-like sheet, which is less pronounced at TiN(100)/a-GeSe and TiN(111)/a-C interfaces. Such a planar-like layer can be rationalized as the strong bond interactions between Ti and Se/Ge atoms. The formation of a Ti-Se layer at TiN/a-GeSe was also observed in previous experimental works [16]. The equilibrium interlayer distances, defined as the distance between the top atomic-layer of TiN substrate and the bottom atomic-layer of a-GeSe (a-C) component, are summarized in Table 2.

The average interfacial distance at TiN(111)/a-GeSe and Ti(100)/a-GeSe is 2.08 Å and 2.48 Å, respectively, while the distance at TiN(111)/a-C is 1.32 Å, which all being much smaller than the interfacial distances found in typical vdW heterostructures [43,44]. This indicates the formation of chemical bonds at interfaces.

To evaluate the interface stability, we calculated the binding energy, E_b, as following:

$$E_b = \frac{E_{int} - \sum_i^2 E_i}{S} \quad (1)$$

where, E_{int} is the total energy of the interface, E_i is the total energy of the two separate components, and S is the contact area at the interface. E_b ranges from −83 meV/A^2 to −364 meV/A^2 (Table 1), close to the values reported for TiN/Al heterostructure [45]. The negative values of E_b implies that the contact interfaces are exothermic (i.e. thermodynamically stable). The amorphous structures are more strongly adsorbed on TiN(111) than on TiN(100) surface, in agreement with the observation that the TiN(111) facet is chemically more reactive [40].

Overall, the calculated values of interlayer distance and binding energy point out that the adsorption of a-GeSe and a-C slabs on TiN surfaces can be classified into the strong chemical bonding interactions, which exert a dramatic effect on the resulting interfacial properties of heterostructures with respect to their constituent components [46,47].

To further analyze the bonding path at the interface, we calculated the bond lengths of Ti—Se, Ti—Ge, N—Ge, N—Se, Ti—C as in the percentage of the van der Waals radii of constituting atoms according to the bonding tetrahedron reported in Refs [48,49]. According to bonding tetrahedron [48], the values of the bond lengths that lie between 70 % and 95 % are considered as the van der Waals gap. The calculated results are summarized in Table S1 of SI: no bond in our heterostructures exceeds the van der Waals limit. In contrast, it is found that all bond lengths at the interface are less than 63 % of the sum of vdW radii of the constituting atoms, which is a typical indication of covalent and ionic bond mixing. The bond lengths at TiN(111)/a-GeSe are shorter than that found at TiN(100)/a-GeSe, which supports the interpretation of stronger interactions with TiN(111)-surface, in line with the binding energy values. The reduction of the a-GeSe thickness (1 nm vs 3 nm) does not have a significant impact on the bond length and binding energy.

The Ti diffusion inhibition into the chalcogenide layer can now be qualitatively explained by the analysis of the Radial Distribution Function (RDF or $g(r)$). The height of the first peak of the RDF is proportional to the bond strength between atoms using the Boltzmann Inversion method [50], where the interatomic potential U(r) is linked to the RDF through the expression:

$$U(r) = -k_B T ln[g(r)] \quad (2)$$

The direct consequence of this relation is that higher the peak, stronger the bond. On the basis of the calculated RDF at the interface, two considerations can be drawn: i) Ti-Ge and Ti-Se bonds show a higher height of the first peak of the g(r) than Ti-C bonds, suggesting the propensity of Ti to interact with Ge/Se with respect to C (**Fig. S3a)**, while the shorter range of the C—C peak (**Fig. S3b)** indicates a higher atomic density of the a-C layer. ii) When TiN interacts directly with GeSe, a layer of both Ge and Se is created at the interface, leaving a small spatial gap between TiN and the GeSe layers. On the contrary, when TiN interacts with a-C, there is no formation of a carbon layer at the interface. This supports the conclusion that Ti atoms can diffuse easier into a-GeSe layer than into the denser a-C bulk. Notably, this is mostly an ionic effect (i.e. higher atomic density) rather than an electronic screening one. This provides a microscopic interpretation of the beneficial Ti-blocking effect of the a-C inclusion, observed in the experimental setup.

The electron density of states (DOS) along with the inverse participation ratio (IPR), summarized in **Fig. S4**, shows that the amorphous structures are characterized by a considerable amount of trap states within the mobility band gap that are localized in energy around the Fermi level (E_F) and localized over a subset of a few connected atoms. These results closely reproduce the electronic structure properties of the a-GeSe bulk case [29], especially for the 3 nm-thick-layer case. The values of mobility gap are defined as the energy difference between the highest occupied continuously delocalized states and the lowest unoccupied continuously delocalized states in the DOS (**Fig. S4**) and are found to be 1.2 eV for a-GeSe, in good agreement with previous DFT calculations and experimental results [27].

In contrast, the a-C layer exhibits a gapless metallic-like behavior with highly delocalized trap states around the Fermi level. In order to make evident the formation of the TiN/a-GeSe (or TiN/a-C) bonds, we calculated 3D charge density difference ($\Delta\rho$), which is defined as the difference between the charge of the heterostructures and the sum of the charges of individual a-GeSe (or a-C) and individual TiN substrate with the same atomic positions, namely, $\Delta\rho = \rho_{int} - \rho_{TiN} - \rho_{a-GeSe/a-C}$. As shown in the left-hand panels of Fig. 3**a** and **Fig. S5** of SI, charge accumulates in the a-GeSe (a-C) part while it depletes in the TiN part of the interface.

We calculated the 2D plane-averaged electron density difference, $\Delta\rho_z$, along the direction perpendicular to the interface, as shown in the right-hand panels of Fig. 3**a** and **Fig. S5**. The large charge density at interface indicates a strong overlap of electron orbitals of atoms at interface. $\Delta\rho_z$ value for TiN(111)/a-GeSe interface is higher than for the TiN(100)/a-GeSe one. This further confirms the stronger chemical interfacial interactions and higher reactivity of the TiN(111) surface.

The charge redistribution at the interface gives rise to a permanent interfacial dipole, which modifies the band alignment of the constituent components and the interfacial Schottky/Ohmic barrier.

The Schottky barrier height for electrons can be estimated by using

Table 2
Calculated values of interlayer distance d (Å), binding energy E_b (meV/Å^2), Schottky barrier height (eV) and ΔV is the total potential step at interfaces (eV); BD is the bond-dipole potential $\Delta V_{a\text{-}GeSe/a\text{-}C}$ is the contribution related to the shift of the electron affinity E_a of the individual semiconductor components, ΔV is the shift from the work function of substrate (TiN).

Interfaces	d (Å)	E_b (meV/ Å^2)	Φn (eV)	Φp (eV)	ΔV (eV)	ΔV_{TiN} (eV)	$\Delta V_{a\text{-}GeSe}$ (eV)	BD (eV)
TiN(111)/a-GeSe-1 nm	2.13	−264.54	0.85	0.27	−0.01	−0.03	−0.54	0.56
TiN(111)/a-GeSe-3 nm	2.08	−297.65	0.54	0.74	−0.29	−0.02	−1.17	0.89
TiN(100)/a-GeSe-1 nm	2.16	−83.39	0.91	0.21	1.41	−0.22	−0.22	1.85
TiN(100)/a-GeSe-3 nm	2.58	−96.22	0.79	0.49	1.34	−0.20	−0.73	2.27
TiN(111)/a-C-3 nm	1.31	−364.47	–	–	0.51	−0.02	−1.11	1.69
a-C-3 nm/ a-GeSe-3 nm	1.02	−390.44	0.30	0.99	0.25	–	−0.61/-0.23	0.61

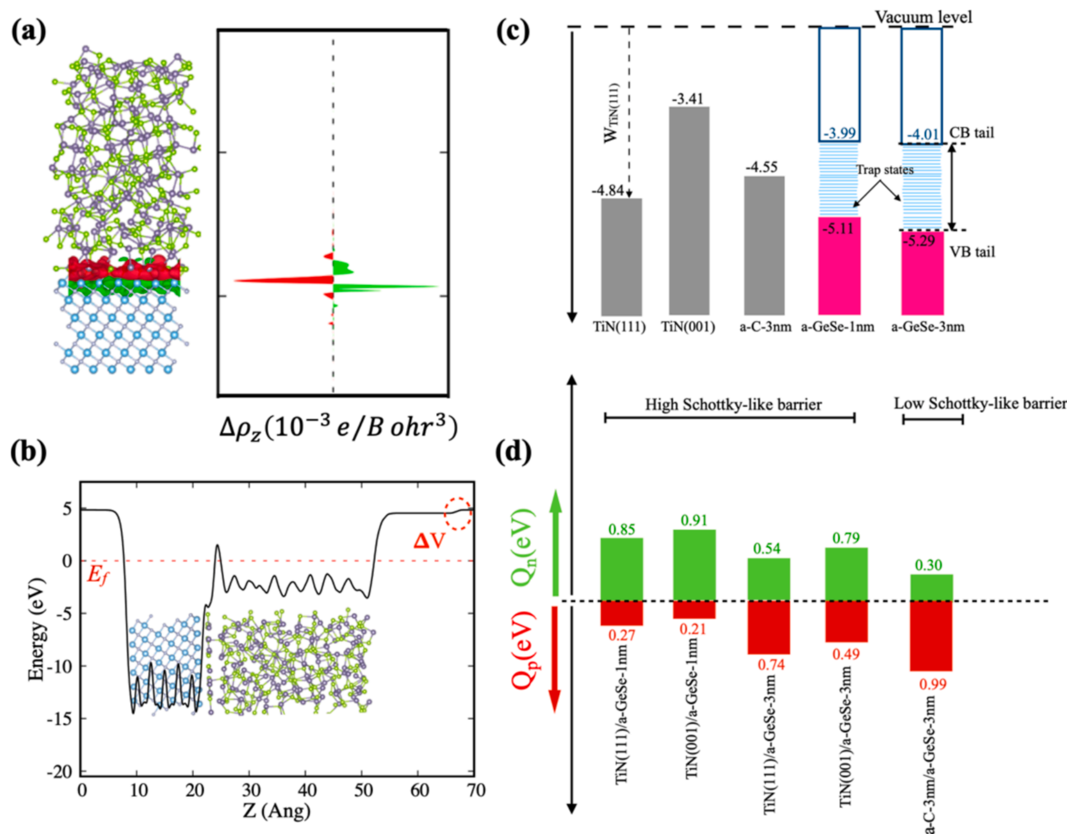

Fig. 3. (a) Left-hand panels show the 3D charge density difference ($\Delta\rho$) at the interface region and right-hand panels show the plane-averaged electron density difference $\Delta\rho_z$ along the direction perpendicular to the interface, (b) The plane-averaged electrostatic potential at interface for TiN(111)/a-GeSe heterostructures, (c) Band alignment of isolated components, the vacuum level is set to zero, and (d) the value of p/n Schottky barrier height (SBH), the fermi level of heterostructure is set to zero.

the same scheme as in Refs [46,47]:

$$Q_n = W_{TiN} - E_{a(a-GeSe/a-C)} + \Delta\Delta V \tag{3}$$

$$Q_n + Q_p = E_g \tag{4}$$

where E_a is the electron affinity of either a-GeSe or a-C slab, W_{TiN} is the work function of TiN substrate, ΔV is the potential drop at interface, and E_g is the mobility gap of isolated amorphous components. From the equation (3), the E_a and W_{TiN} can be easily obtained in the separate calculations on the isolated a-GeSe slabs and the clean metal surfaces. The ΔV step is evaluated from the average potential profile across the interface of heterostructures as shown in Fig. 3**b and Fig. S6**. The potential step does not critically depend on the DFT functional and can be calculated without resorting to the details of the potential profile across the interface or its electronic structure [51,52].

We first analyze the band edge alignment of the free-standing components. Fig. 3**c** shows the frontier of band edges of separate TiN substrate, a-GeSe and a-C structures. The calculated values of the work function of TiN(100) and TiN(111) surfaces, defined as the energy difference between the E_F and vacuum level, are 3.4 and 4.84 eV, respectively. These values by vdW-DF-optB86b functional are larger only by 0.2–0.4 eV than those obtained at GGA-PBE level [40]. Nevertheless, the *WF* values are in the range of the reasonable average experimental work function values of 4.74 eV reported for TiN surface. The work function of TiN is very sensitive to preparation and environmental conditions [40,53,54], as well as to the exposed surface face. The band alignment of the separate sub-systems indicates that the TiN(111) *WF* lies in the mobility gap of the semiconductor counterpart. This indicates that, at an infinite interlayer distance, the TiN(111) would develop a p-/n-type Schottky-like barrier with a-GeSe and in a heterostructure stack.

When the effect of the charge transfer, due to bond formation at the interface, is considered this scenario changes. The calculated values of SBHs (Q_n and Q_p) for the different interfaces are summarized in Fig. 3**d**. These results indicate that the a-GeSe slabs form a n/p type Schottky contact with TiN for both surface orientations (100) and (111), in line with the experimental values discussed below. The values of Q_n and Q_p can be modulated by changing the orientation of TiN substrate and the thickness of amorphous systems. Most importantly, the insertion of the a-C buffer layer forms a small Schottky barrier with a-GeSe. The low SBH for electrons as the a-GeSe/a-C interface leads to a higher leakage current, contributing to a lower V_{TH}, see also Fig. 4.

The difference in the features of SBH contact with respect to the single components can be explained in terms of the modification of the band alignment at the interface (work function of metal and band edges of semiconductor), mainly due to a potential step ΔV, as shown in Fig. 3**b and Fig. S5**. The variation of ΔV step is associated to many contributions: (i) the interface dipole due to charge redistribution across the interface which is usually referred as the bond-dipole potential (*BD*), (ii) the contribution stemming from the shift in the electron affinity E_a of the individual semiconductor components, $\Delta V_{a\text{-}GeSe/a\text{-}C}$, and (iii) the change of the work function of substrate (ΔV_{TiN}) due to the geometrical reconstruction at the heterostructure interface [55,56]. Altogether, the total potential step at interface can be described by the summation of these three quantities:

$$\Delta V = \Delta V_{TiN} + \Delta V_{a-GeSe/a-C} + BD \tag{5}$$

The ΔV_{TiN} and $\Delta V_{a\text{-}GeSe/a\text{-}C}$ values can be extracted from the modification of the electrostatic potential profiles between the individual components in the relaxed heterostructure and in the isolated components, see **Fig. S7** in SI. The *BD* contribution can be estimated

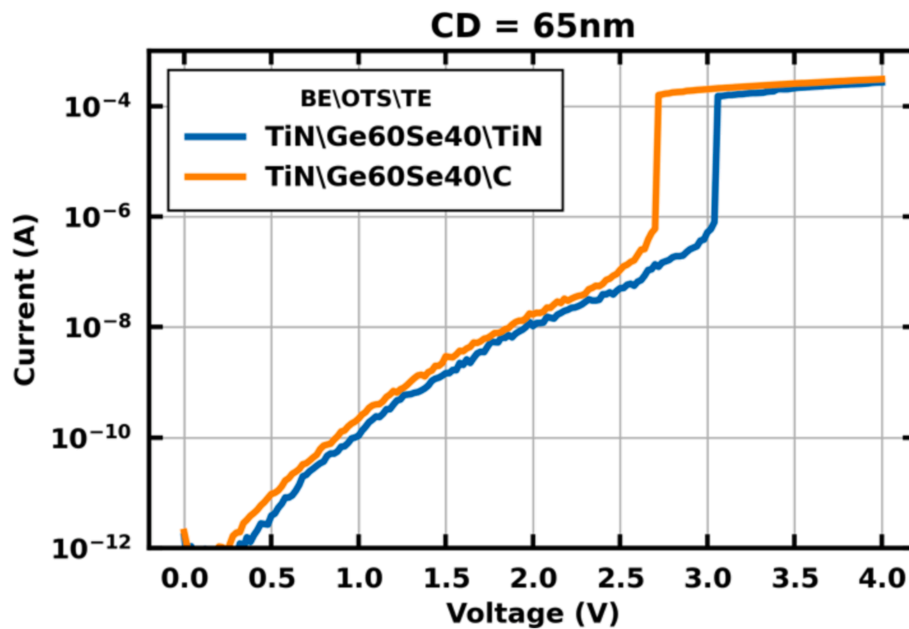

Fig. 4. I-V characteristics of the TiN/a-GeSe and TiN/ a-GeSe/a-C/TiN devices.

numerically by solving the Poisson equation on the charge density difference at the interface, $\Delta\rho_z$ as described in Fig. 3**a and Fig. S5**. The calculated terms entering in Eq. (5) and the total potential step ΔV are summarized in Table 2. All the terms due to the geometrical rearrangement have negative values ranging from -0.02 to -1.17 eV, which significantly contribute to the modification in contact barriers at the interface. The potential shift associated with the structural reorganization of TiN(111) and TiN(100) surfaces is small (< 0.2 eV) in all cases of interfaces. This is due to the fact that TiN surfaces are structurally stable and only slightly affected by the interactions with amorphous material. The contribution arising from the amorphous components, $\Delta V_{a\text{-}GeSe/a\text{-}C}$ (or $\Delta V_{a\text{-}C}$) is remarkable and directly associated to the atomic rearrangement of atoms at the interface with respect to the a-GeSe, (a-C) bulk as shown in **Fig. S7**. The larger contribution is found for the a-GeSe (a-C) component in the TiN(111)/a-GeSe (TiN(111)/a-C) heterostructure configuration. Reducing the thickness of a-GeSe slab decreases the contribution from the $\Delta V_{a\text{-}GeSe}$. In contrast, the contribution from the bond-dipole coupling is positive for all heterostructures, indicating that the interfacial dipole is oriented from the amorphous components towards the TiN substrate. The values of *BD* are found to be larger for TiN (100)/a-GeSe than for TiN(111)/a-GeSe stack.

3.2. Experimental devices characterization

In Fig. 4 we report the current–voltage measured on TiN and TiN/a-C electrodes devices with a-GeSe obtained by PVD. The threshold voltage (V_{TH}) for the TiN electrodes is about 3.0 V. The addition of a-C electrode results in slightly increased I_{off} current and showing a lower threshold voltage by about 0.3 V, while preserving the Schottky type contact. The experimental measurements support our theoretical predictions that the a-C interface lowers the electron injection barrier (SBH), therefore leading to lower V_{TH}.

By comparing the mobility gap of the $Ge_{40}Se_{60}/Ge_{60}Se_{40}$ compositions from [41], we conclude that higher Ge content causes a lower effective mobility gap [27,57], which corresponds to lower Schottky barriers for charge injection [41]. Moreover, previous theoretical simulations of the electrical characteristics (e.g. I-V and G-V) of the two terminal TiN/a-GeSe/TiN device [27] indicated that the transport mechanism is mainly due to multi-phonon defect-assisted trap mechanisms which include trap-to-trap (major) and trap-to-band (minor) contributions. The measured V_{TH} and I_{off} on the $Ge_{60}Se_{40}$ samples, therefore, are expected to represent the upper boundary in the $Ge_{40}Se_{60}/Ge_{60}Se_{40}$ series, i.e., lower leakage and higher threshold voltages are expected in $Ge_{40}Se_{60}/Ge_{50}Se_{50}$ compositions, in agreement with the theoretical results discussed above.

4. Conclusion

We have theoretically and experimentally characterized the interface between GeSe (a-C) amorphous materials and TiN metallic substrate. Both a-GeSe and a-C amorphous materials interact strongly with TiN substrate via chemical bonds, which results in a significant modification of the band alignment at the interface. Both experimental and theoretical results concur in attributing to a Schottky-type character to the TiN/ a-GeSe contact. The insertion of a a-C buffer layer between a-GeSe and TiN substrate yields a significant enhancement of V_{TH}, while the denser C—C bonds hinders the Ti-diffusion across the interface. The DFT calculations demonstrated that the contact between a-C and TiN substrate is Ohmic like, which ensures an electrical current flow without any significant potential drops. These electrical characteristics can be mainly rationalized at the microscopic level the establishment of of dipole–dipole interaction across the interface. Moreover, the interface between a-GeSe and a-C is found to be band alignment type-II. While the device stability under several ON/OFF cycles remains a technological issue to be solved [58], our results indicate that the inclusion of thin C-buffer layers provides a useful strategy to control the interface quality in OTS switches, that can be easily integrated in large scale production processes.

CRediT authorship contribution statement

Amine Slassi: Writing – original draft, Validation, Investigation. **Francesco Tavanti:** Writing – review & editing, Supervision. **Sergiu Clima:** Supervision, Conceptualization. **Daniele Garbin:** Writing – original draft, Validation, Investigation. **Arrigo Calzolari:** Supervision, Conceptualization.

Funding

This work was supported by the OPENMODEL project (EU Project

H2020-NMBP-953167) .

Declaration of competing interest

The authors declare that they have no known competing financial interests or personal relationships that could have appeared to influence the work reported in this paper.

Acknowledgements

We sincerely thank Dr. Ben Kaczer for useful and fruitful discussion.

Appendix A. Supplementary data

Supplementary data to this article can be found online at https://doi.org/10.1016/j.apsusc.2025.162455.

Data availability

Data will be made available on request.

References

[1] W. Zhang, R. Mazzarello, M. Wuttig, E. Ma, Designing crystallization in phase-change materials for universal memory and neuro-inspired computing, Nat. Rev. Mater. 4 (2019) 150–168, https://doi.org/10.1038/s41578-018-0076-x.
[2] G.W. Burr, M.J. Breitwisch, M. Franceschini, D. Garetto, K. Gopalakrishnan, B. Jackson, B. Kurdi, C. Lam, L.A. Lastras, A. Padilla, B. Rajendran, S. Raoux, R. S. Shenoy, Phase change memory technology, J. Vac. Sci. Technol. B 28 (2010) 223–262, https://doi.org/10.1116/1.3301579.
[3] DerChang Kau, S. Tang, I. V. Karpov, R. Dodge, B. Klehn, J. A. Kalb, J. Strand, A. Diaz, N. Leung, J. Wu, Sean Lee, T. Langtry, Kuo-wei Chang, C. Papagianni, Jinwook Lee, J. Hirst, S. Erra, E. Flores, N. Righos, H. Castro, G. Spadini, A stackable cross point Phase Change Memory, in: 2009 IEEE International Electron Devices Meeting (IEDM), 2009: pp. 1–4. Doi: 10.1109/IEDM.2009.5424263.
[4] T. Kim, H. Choi, M. Kim, J. Yi, D. Kim, S. Cho, H. Lee, C. Hwang, E.-R. Hwang, J. Song, S. Chae, Y. Chun, J.-K. Kim, High-performance, cost-effective 2z nm two-deck cross-point memory integrated by self-align scheme for 128 Gb SCM, in: In: 2018 IEEE International Electron Devices Meeting (IEDM), 2018, https://doi.org/10.1109/IEDM.2018.8614680.
[5] V. Adinolfi, L. Cheng, M. Laudato, R.C. Clarke, V.K. Narasimhan, S. Balatti, S. Hoang, K.A. Littau, Composition-controlled atomic layer deposition of phase-change memories and ovonic threshold switches with high performance, ACS Nano 13 (2019) 10440–10447, https://doi.org/10.1021/acsnano.9b04233.
[6] F.T. Hady, A. Foong, B. Veal, D. Williams, Platform storage performance with 3D XPoint technology, Proc. IEEE. (2017) 1051822–1051833, https://doi.org/10.1109/JPROC.2017.2731776.
[7] D. Loke, T.H. Lee, W.J. Wang, L.P. Shi, R. Zhao, Y.C. Yeo, T.C. Chong, S.R. Elliott, Breaking the speed limits of phase-change memory, Science 336 (2012) 1566–1569, https://doi.org/10.1126/science.1221561.
[8] Y.-H. Lee, P.J. Liao, V. Hou, D. Heh, C.-H. Nien, W.-H. Kuo, G.T. Chen, S.-M. Yu, Y.-S. Chen, J.-Y. Wu, X. Bao, C.H. Diaz, Composition segregation of Ge-Rich GST and its effect on reliability, IEEE International Reliability Physics Symposium (IRPS) (2021) 1–6, https://doi.org/10.1109/IRPS46558.2021.9405168.
[9] R.E. Simpson, P. Fons, A.V. Kolobov, T. Fukaya, M. Krbal, T. Yagi, J. Tominaga, Interfacial phase-change memory, Nat. Nanotechnol. 6 (2011) 501–505, https://doi.org/10.1038/nnano.2011.96.
[10] Y. Zhou, W. Zhang, E. Ma, V.L. Deringer, Device-scale atomistic modelling of phase-change memory materials, Nature Electronics 6 (2023) 746–754, https://doi.org/10.1038/s41928-023-01030-x.
[11] Z. Chai, W.D. Zhang, R. Degraeve, S. Clima, F. Hatem, J.F. Zhang, P. Freitas, J. Marsland, A. Fantini, D. Garbin, L. Goux, G.S. Kar, Dependence of switching probability on operation conditions in GexSe1-x ovonic threshold switching selectors, IEEE Electron Device Lett. (2019), https://doi.org/10.1109/led.2019.2924270.
[12] D.S. Jeong, H. Lim, G.-H. Park, C.S. Hwang, S. Lee, B. Cheong, Threshold resistive and capacitive switching behavior in binary amorphous GeSe, J. Appl. Phys. 111 (2012) 102807, https://doi.org/10.1063/1.4714705.
[13] H.-W. Ahn, D.S. Jeong, B. Cheong, S. Kim, S.-Y. Shin, H. Lim, D. Kim, S. Lee, A study on the scalability of a selector device using threshold switching in Pt/GeSe/Pt, ECS Solid State Lett. 2 (2013) N31, https://doi.org/10.1149/2.011309ssl.
[14] F. Tavanti, A. Calzolari, Concurring effect of doping and composition on the thermodynamic properties of amorphous GexSe1-x alloys, Acta Mater. 266 (2024) 119676, https://doi.org/10.1016/j.actamat.2024.119676.
[15] S.R. Ovshinsky, Reversible electrical switching phenomena in disordered structures, Phys. Rev. Lett. 21 (1968) 1450–1453, https://doi.org/10.1103/PhysRevLett.21.1450.
[16] W. Kim, C. Yoo, E.-S. Park, M. Ha, J.W. Jeon, G.S. Kim, K.S. Woo, Y.K. Lee, C. S. Hwang, Electroforming-free bipolar resistive switching in GeSe thin films with a Ti-containing electrode, ACS Appl. Mater Interfaces 11 (2019) 38910–38920, https://doi.org/10.1021/acsami.9b10891.
[17] C. Yoo, W. Kim, J.W. Jeon, E.-S. Park, M. Ha, Y.K. Lee, C.S. Hwang, Atomic layer deposition of GexSe1–x thin films for endurable ovonic threshold selectors with a low threshold voltage, ACS Appl. Mater. Interfaces 12 (2020) 23110–23118, https://doi.org/10.1021/acsami.0c03747.
[18] A. Haider, S. Deng, W. Devulder, J.W. Maes, J.-M. Girard, G. Khalil El Hajjam, G. S. Kar, K. Opsomer, C. Detavernier, M. Givens, L. Goux, S. Van Elshocht, R. Delhougne, A. Delabie, M. Caymax, J. Swerts, Pulsed chemical vapor deposition of conformal GeSe for application as an OTS selector, Mater. Adv. 2 (2021) 1635–1643, https://doi.org/10.1039/D0MA01014F.
[19] A. Verdy, G. Navarro, M. Bernard, S. Chevalliez, N. Castellani, E. Nolot, J. Garrione, P. Noé, G. Bourgeois, V. Sousa, M.-C. Cyrille, E. Nowak, Carbon electrode for Ge-Se-Sb based OTS selector for ultra low leakage current and outstanding endurance, in: In: 2018 IEEE International Reliability Physics Symposium (IRPS), 2018, https://doi.org/10.1109/IRPS.2018.8353635.
[20] X. Yang, B. Tian, M. Jian, M. Wu, W. Li, J. Jiang, Z. Guo, L. Yang, Molecular dynamics simulation of uniaxial stretching for silicon nitride deposited by PECVD, Appl. Surf. Sci. 682 (2025) 161696, https://doi.org/10.1016/j.apsusc.2024.161696.
[21] Z. Li, J. Han, S. Cao, Z. Zhang, X. Deng, Physical properties of monolayer Mn (BiTeS)2 and its applications in sub–3 nm spintronic devices, Phys. Rev. B 108 (2023) 184413, https://doi.org/10.1103/PhysRevB.108.184413.
[22] Z. Li, J. Han, S. Cao, Z. Zhang, X. Deng, First-principles study of metal-semiconductor contacts and quantum transport simulations for 5.1-nm monolayer MoSi2N4 devices, PhysRevAppli 21 (2024) 054062, https://doi.org/10.1103/PhysRevApplied.21.054062.
[23] C. He, J. Ma, S. Xi, W. Zhang, “Blocking and rebalance” mechanism-guided design strategies of bimetallic doped 2D α-phosphorus carbide as efficient catalysts for N2 electroreduction, J. Energy Chem. 97 (2024) 68–78, https://doi.org/10.1016/j.jechem.2024.05.040.
[24] W. Zhang, X. He, C. He, The “d-p orbital hybridization”-guided design of novel two-dimensional MOFs with high anchoring and catalytic capacities in Lithium − Sulfur batteries, J. Colloid Interface Sci. 678 (2025) 540–548, https://doi.org/10.1016/j.jcis.2024.08.184.
[25] W.X. Zhang, S.L. Kong, W.W. Wang, Y.M. Cheng, Z. Li, C. He, Enhanced electrocatalytic performance of LCO-NiFe-C3N4 composite material for highly efficient overall water splitting, J. Colloid Interface Sci. 680 (2025) 787–796, https://doi.org/10.1016/j.jcis.2024.11.118.
[26] N.S. Avasarala, G.L. Donadio, T. Witters, K. Opsomer, B. Govoreanu, A. Fantini, S. Clima, H. Oh, S. Kundu, W. Devulder, M.H. van der Veen, J. Van Houdt, M. Heyns, L. Goux, G.S. Kar, Half-threshold bias Ioff reduction down to nA range of thermally and electrically stable high-performance integrated OTS selector, obtained by Se enrichment and N-doping of thin GeSe layers, IEEE Symposium on VLSI Technol. (2018) 209–210, https://doi.org/10.1109/VLSIT.2018.8510680.
[27] A. Slassi, L.-S. Medondjio, A. Padovani, F. Tavanti, X. He, S. Clima, D. Garbin, B. Kaczer, L. Larcher, P. Ordejón, A. Calzolari, Device-to-materials pathway for electron traps detection in amorphous GeSe-based selectors, Adv. Electron. Mater. 9 (2023) 2201224, https://doi.org/10.1002/aelm.202201224.
[28] J. Keukelier, K. Opsomer, W. Devulder, S. Clima, L. Goux, G. Sankar Kar, C. Detavernier, Tuning of the thermal stability and ovonic threshold switching properties of GeSe with metallic and non-metallic alloying elements, J. Appl. Phys. 130 (2021) 165103, https://doi.org/10.1063/5.0055861.
[29] P. Giannozzi, O. Andreussi, T. Brumme, O. Bunau, M. Buongiorno Nardelli, M. Calandra, R. Car, C. Cavazzoni, D. Ceresoli, M. Cococcioni, N. Colonna, I. Carnimeo, A. Dal Corso, S. de Gironcoli, P. Delugas, R.A. DiStasio, A. Ferretti, A. Floris, G. Fratesi, G. Fugallo, R. Gebauer, U. Gerstmann, F. Giustino, T. Gorni, J. Jia, M. Kawamura, H.-Y. Ko, A. Kokalj, E. Küçükbenli, M. Lazzeri, M. Marsili, N. Marzari, F. Mauri, N.L. Nguyen, H.-V. Nguyen, A. Otero-de-la-Roza, L. Paulatto, S. Poncé, D. Rocca, R. Sabatini, B. Santra, M. Schlipf, A.P. Seitsonen, A. Smogunov, I. Timrov, T. Thonhauser, P. Umari, N. Vast, X. Wu, S. Baroni, Advanced capabilities for materials modelling with Quantum ESPRESSO, J. Phys. Condens. Matter 29 (2017) 465901, https://doi.org/10.1088/1361-648X/aa8f79.
[30] D. Vanderbilt, Soft self-consistent pseudopotentials in a generalized eigenvalue formalism, Phys. Rev. B 41 (1990) 7892–7895, https://doi.org/10.1103/PhysRevB.41.7892.
[31] A. Tverjanovich, M. Khomenko, C.J. Benmore, M. Bokova, A. Sokolov, D. Fontanari, M. Kassem, T. Usuki, E. Bychkov, Bulk glassy GeTe2: a missing member of the tetrahedral GeX2 family and a precursor for the next generation of phase-change materials, Chem. Mater. 33 (2021) 1031–1045, https://doi.org/10.1021/acs.chemmater.0c04409.
[32] V.R. Cooper, Van der Waals density functional: an appropriate exchange functional, Phys. Rev. B 81 (2010) 161104, https://doi.org/10.1103/PhysRevB.81.161104.
[33] J. Klimeš, D.R. Bowler, A. Michaelides, Van der Waals density functionals applied to solids, Phys. Rev. B 83 (2011) 195131, https://doi.org/10.1103/PhysRevB.83.195131.
[34] W. Zhang, A. Thiess, P. Zalden, R. Zeller, P.H. Dederichs, J.-Y. Raty, M. Wuttig, S. Blügel, R. Mazzarello, Role of vacancies in metal–insulator transitions of crystalline phase-change materials, Nat. Mater. 11 (2012) 952–956, https://doi.org/10.1038/nmat3456.
[35] A.P. Thompson, H.M. Aktulga, R. Berger, D.S. Bolintineanu, W.M. Brown, P. S. Crozier, P.J. in 't Veld, A. Kohlmeyer, S.G. Moore, T.D. Nguyen, R. Shan, M. J. Stevens, J. Tranchida, C. Trott, S.J. Plimpton, LAMMPS - a flexible simulation tool for particle-based materials modeling at the atomic, meso, and continuum

scales, Comput. Phys. Commun. 271 (2022) 108171, https://doi.org/10.1016/j.cpc.2021.108171.
[36] F. Tavanti, B. Dianat, A. Catellani, A. Calzolari, Hierarchical short- and medium-range order structures in amorphous GexSe1−x for selectors applications, ACS Appl. Electron. Mater. 2 (2020) 2961–2969, https://doi.org/10.1021/acsaelm.0c00581.
[37] J. Tersoff, Empirical interatomic potential for carbon, with applications to amorphous carbon, Phys. Rev. Lett. 61 (1988) 2879–2882, https://doi.org/10.1103/PhysRevLett.61.2879.
[38] F. Buscemi, E. Piccinini, L. Vandelli, F. Nardi, A. Padovani, B. Kaczer, D. Garbin, S. Clima, R. Degraeve, G.S. Kar, F. Tavanti, A. Slassi, A. Calzolari, L. Larcher, A hydrodynamic model for trap-assisted tunneling conduction in ovonic devices, IEEE Trans. Electron Devices 70 (2023) 1808–1814, https://doi.org/10.1109/TED.2023.3242229.
[39] A. Catellani, A. Calzolari, Plasmonic properties of refractory titanium nitride, Phys. Rev. B 95 (2017) 115145, https://doi.org/10.1103/PhysRevB.95.115145.
[40] A. Calzolari, A. Catellani, Controlling the TiN electrode work function at the atomistic level: a first principles investigation, IEEE Access 8 (2020) 156308–156313, https://doi.org/10.1109/ACCESS.2020.3017726.
[41] S. Clima, D. Garbin, K. Opsomer, N.S. Avasarala, W. Devulder, I. Shlyakhov, J. Keukelier, G.L. Donadio, T. Witters, S. Kundu, B. Govoreanu, L. Goux, C. Detavernier, V. Afanas'ev, G.S. Kar, G. Pourtois, Ovonic threshold-switching gexsey chalcogenide materials: stoichiometry, trap nature, and material relaxation from first principles, Physica Status Solidi (RRL) – Rapid Research Letters 14 (2020) 1900672, https://doi.org/10.1002/pssr.201900672.
[42] M. Marlo, V. Milman, Density-functional study of bulk and surface properties of titanium nitride using different exchange-correlation functionals, Phys. Rev. B 62 (2000) 2899–2907, https://doi.org/10.1103/PhysRevB.62.2899.
[43] A. Slassi, J. Cornil, Theoretical characterization of strain and interfacial electronic effects in donor-acceptor bilayers of 2D transition metal dichalcogenides, 2D Materials 6 (2018) 015025, https://doi.org/10.1088/2053-1583/aaf1d4.
[44] A. Slassi, D. Cornil, J. Cornil, Theoretical characterization of the electronic properties of heterogeneous vertical stacks of 2D metal dichalcogenides containing one doped layer, Phys. Chem. Chem. Phys. 22 (2020) 14088–14098, https://doi.org/10.1039/D0CP01878C.
[45] G. Feldbauer, M. Wolloch, P.O. Bedolla, P. Mohn, J. Redinger, A. Vernes, Adhesion and material transfer between contacting Al and TiN surfaces from first principles, Phys. Rev. B 91 (2015) 165413, https://doi.org/10.1103/PhysRevB.91.165413.
[46] A. El Haimeur, A. Slassi, A. Pershin, D. Cornil, M. Makha, E. Blanco, M. Dominguez, H. Bakkali, Reducing p-type Schottky contact barrier in metal/ZnO heterostructure through Ni-doping, Appl. Surf. Sci. 545 (2021) 149023, https://doi.org/10.1016/j.apsusc.2021.149023.
[47] A. Slassi, P.B. Sorokin, A. Pershin, Ohmic/Schottky barrier engineering in metal/SnP3 heterostructures, J. Alloy. Compd. 831 (2020) 154800, https://doi.org/10.1016/j.jallcom.2020.154800.
[48] A.H. Woomer, D.L. Druffel, J.D. Sundberg, J.T. Pawlik, S.C. Warren, Bonding in 2D donor–acceptor heterostructures, J. Am. Chem. Soc. 141 (2019) 10300–10308, https://doi.org/10.1021/jacs.9b03155.
[49] A. Slassi, S.M. Gali, A. Pershin, A. Gali, J. Cornil, D. Beljonne, Interlayer bonding in two-dimensional materials: the special case of SnP3 and GeP3, J. Phys. Chem. Lett. 11 (2020) 4503–4510, https://doi.org/10.1021/acs.jpclett.0c00780.
[50] T.C. Moore, C.R. Iacovella, C. McCabe, Derivation of coarse-grained potentials via multistate iterative Boltzmann inversion, J. Chem. Phys. 140 (2014) 224104, https://doi.org/10.1063/1.4880555.
[51] M. Farmanbar, G. Brocks, Controlling the Schottky barrier at MoS2/metal contacts by inserting a BN monolayer, Phys. Rev. B 91 (2015) 161304, https://doi.org/10.1103/PhysRevB.91.161304.
[52] M. Farmanbar, G. Brocks, First-principles study of van der Waals interactions and lattice mismatch at MoS2/metal interfaces, PhysRevB 93 (2016) 085304, https://doi.org/10.1103/PhysRevB.93.085304.
[53] F. Fillot, T. Morel, S. Minoret, I. Matko, S. Maîtrejean, B. Guillaumot, B. Chenevier, T. Billon, Investigations of titanium nitride as metal gate material, elaborated by metal organic atomic layer deposition using TDMAT and NH3, Microelectron. Eng. 82 (2005) 248–253, https://doi.org/10.1016/j.mee.2005.07.083.
[54] J. Westlinder, T. Schram, L. Pantisano, E. Cartier, A. Kerber, G.S. Lujan, J. Olsson, G. Groeseneken, On the thermal stability of atomic layer deposited TiN as gate electrode in MOS devices, IEEE Electron Device Lett. 24 (2003) 550–552, https://doi.org/10.1109/LED.2003.816579.
[55] G. Heimel, F. Rissner, E. Zojer, Modeling the electronic properties of π-conjugated self-assembled monolayers, Adv. Mater. 22 (2010) 2494–2513, https://doi.org/10.1002/adma.200903855.
[56] D. Cornil, T. Van Regemorter, D. Beljonne, J. Cornil, Work function shifts of a zinc oxide surface upon deposition of self-assembled monolayers: a theoretical insight, Phys. Chem. Chem. Phys. 16 (2014) 20887–20899, https://doi.org/10.1039/C4CP02811B.
[57] S. Clima, F. Ducry, D. Garbin, T. Ravsher, R. Degraeve, A. Belmonte, G. Sankar Kar, G. Pourtois, Selector Only Memory: Exploring Atomic Mechanisms from First-Principles. In: IEEE IEDM 2024, San Francisco, CA, United States, 2024.
[58] P. Fantini, A. Ghetti, E. Varesi, A. Pirovano, D. Baratella, C. Ribaldone, D. Campi, M. Bernasconi, R. Bez, VT window model of the Single-chalcogenide Xpoint Memory (SXM). In: IEEE IEDM 2024, San Francisco, CA, United States, 2024.